International Journal of Nanomedicine

Dovepress
open access to scientific and medical research

Open Access Full Text Article

ORIGINAL RESEARCH

Cellular Uptake of Modified Mesoporous Bioactive Glass Nanoparticles for Effective Intracellular Delivery of Therapeutic Agents

Negar Hassani Besheli[1], Juul Verbakel[1], Maryam Hosseini[1], Lea Andrée[1], Ben Joosten[2],
X Frank Walboomers[1], Alessandra Cambi[2], Fang Yang[1], Sander CG Leeuwenburgh[1]

[1]Department of Dentistry – Regenerative Biomaterials, Radboud Institute for Molecular Life Sciences, Radboudumc, Nijmegen, The Netherlands; [2]Department of Cell Biology, Radboud Institute for Molecular Life Sciences, Radboudumc, Nijmegen, The Netherlands

Correspondence: Sander CG Leeuwenburgh, Tel +31 6 15 40 9006, Fax +31 2 43 61 4657, Email sander.leeuwenburgh@radboudumc.nl

Introduction: There has recently been a surge of interest in mesoporous bioactive glass nanoparticles (MBGNs) as multi-functional nanocarriers for application in bone-reconstructive and -regenerative surgery. Their excellent control over their structural and physicochemical properties renders these nanoparticles suitable for the intracellular delivery of therapeutic agents to combat degenerative bone diseases, such as bone infection, or bone cancer. Generally, the therapeutic efficacy of nanocarriers strongly depends on the efficacy of their cellular uptake, which is determined by numerous factors including cellular features and the physicochemical characteristics of nanocarriers, particularly surface charge. In this study, we have systematically investigated the effect of the surface charge of MBGNs doped with copper as a model therapeutic agent on cellular uptake by both macrophages and pre-osteoblast cells involved in bone healing and bone infections to guide the future design of MBGN-based nanocarriers.

Methods: Cu-MBGNs with negative, neutral, and positive surface charges were synthesized and their cellular uptake efficiency was assessed. Additionally, the intracellular fate of internalized nanoparticles along with their ability to deliver therapeutic cargo was studied in detail.

Results: The results showed that both cell types internalized Cu-MBGNs regardless of their surface charge, indicating that cellular uptake of nanoparticles is a complex process influenced by multiple factors. This similarity in cellular uptake was attributed to the formation of a protein corona surrounding the nanoparticles when exposed to protein-rich biological media, which masks the original nanoparticle surface. Once internalized, the nanoparticles were found to mainly colocalize with lysosomes, exposing them to a more compartmentalized and acidic environment. Furthermore, we verified that Cu-MBGNs released their ionic components (Si, Ca, and Cu ions) in both acidic and neutral environments, leading to the delivery of these therapeutic cargos intracellularly.

Conclusion: The effective internalization of Cu-MBGNs and their ability to deliver cargos intracellularly highlight their potential as intracellular delivery nanocarriers for bone-regenerative and -healing applications.

Keywords: intracellular delivery, nanocarrier, bioactive glass, copper, surface charge

Introduction

In recent years, nanotechnology has emerged as a potent tool to design smart nanocarriers as delivery vehicles for various therapeutic agents. Compared to conventional systemic drug delivery, this local delivery would improve the treatment of clinical complications, including inoperable cancers, persistent infections, and metabolic disorders.[1,2] To this end, various drug delivery nanocarriers (eg, dendrimers, liposomes, quantum dots, inorganic and metallic nanoparticles) have been developed to enhance the bioavailability, therapeutic efficacy, and delivery kinetics of locally administered drugs.[3] Inorganic nanoparticles, in particular silicate-based calcium-doped mesoporous bioactive glass nanoparticles (MBGNs), have recently gained considerable research interest in bone regeneration due to their biocompatibility, bone-bonding ability, and intrinsic bone-regenerative capacity. Moreover, the therapeutic efficacy of MBGNs can be boosted even further by the incorporation of therapeutic ions (eg, Ag, Cu, Te, Sr, and Ce) and biomolecules such as nucleic acids or

Received: 21 November 2022
Accepted: 23 February 2023
Published: 28 March 2023

Graphical Abstract

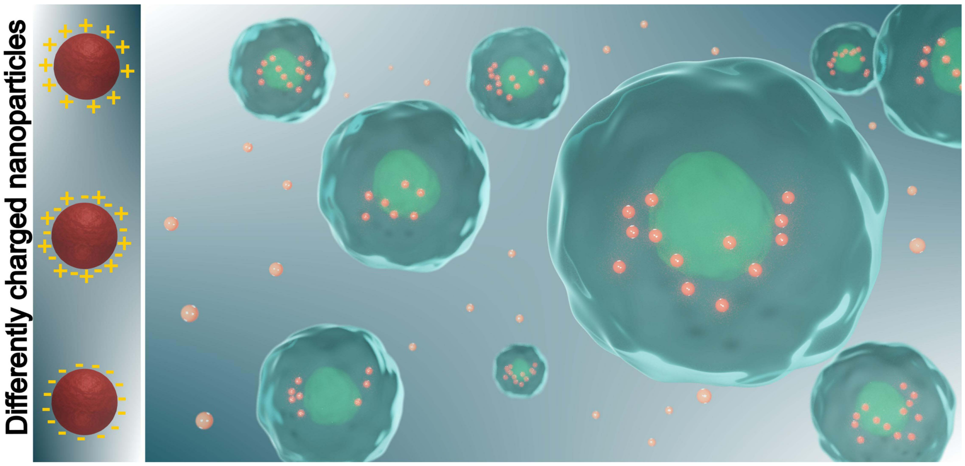

anticancer drugs (eg, doxorubicin). Their tunable mesoporosity in terms of pore size, pore shape, and pore volume, as well as their versatility regarding surface modification, make these nanoparticles highly suitable for targeted and controlled delivery of a wide variety of therapeutic agents. In addition, their tunable nanoscale dimensions enable cellular uptake, which may benefit the development of therapies that strongly rely on nanoparticle internalization.[4–11] Finally, the dissolution rates of MBGNs vary depending on the pH level, resulting in pH-responsive release kinetics of loaded biomolecules. As a result, MBGNs are generally recognized as pH-responsive drug nanocarriers, and their ability to dissolve more rapidly under acidic conditions can be leveraged for targeted delivery of therapeutic agents in pH levels commonly associated with degenerative diseases like bone cancer or bone infection.[11–13] Bone infections, for instance, are often caused by the persistence of intracellular bacterial pathogens, and this results in the therapeutic failure of conventional antibiotics, due to their low cell penetration rates and intracellular retention.[14,15] Therefore, given the advantages of MBGNs described above, these nanocarriers are increasingly advocated as promising nanocarriers for the treatment of bone infection.

However, the therapeutic performance of these nanocarriers for the intracellular delivery of therapeutic agents strongly depends on their cellular uptake efficiency. Cellular uptake is a highly dynamic and complex process modulated by both the physicochemical characteristics of nanocarriers (size, morphology and structure, surface charge, hydrophobicity, surface chemistry, and elasticity) and cellular factors (cell types and physiological state). In addition, these factors determine the mode of uptake which then has a direct effect on the intracellular localization and cytotoxicity of nanoparticles.[16,17] The interaction between nanocarriers and host cells should therefore be optimized to ensure the maximum therapeutic efficacy of intracellular delivery. The surface charge of nanocarriers is considered to be one of the most influential factors controlling nanoparticle internalization and subsequent intracellular drug delivery. Generally, positively charged nanocarriers are assumed to favor nanoparticle internalization due to their attractive electrostatic interactions with the negatively charged cell membrane.[16,18] Among the few studies that investigated the uptake of MBGNs, Lee et al reported that the uptake efficiency of positively charged amine-functionalized MBGNs with a surface charge of +15.3 mV was very high (92%) for rat dental pulp stem cells.[19] However, efficient uptake (~95%) of negatively charged MBGNs (−14.6 mV) of similar size by human multipotent stem cells derived from dental pulp has been reported as well.[8] On the other hand, human osteosarcoma cells (MG63) were unable to internalize Te-MBGNs with a size of 500 nm and negative surface charge (~ −15 mV), which was attributed to excessive nanoparticle aggregation.[5] In contrast, positively charged silica NPs (41±3 mV, 55 ± 2 nm in size) are internalized more efficiently by HeLa cells as compared to their negatively charged analogs (−56±2 mV).[20] These contradictory findings highlight the complexity of the cellular uptake of MBGNs.

Herein we hypothesize that biological fluids strongly alter the physicochemical properties and cellular interactions of the nanoparticles, and in doing so, control the cellular uptake by various cell types.[21] These effects are often overlooked or even completely ignored in the design of nanocarriers for intracellular delivery of therapeutic agents.[8,19,22] Therefore, this study aimed to elucidate the effect of MBGN surface charge on their cellular uptake by different cell types to guide the future design of MBGN-based nanocarriers. To this end, we systematically investigated the internalization of three types of copper-doped MBGNs (Cu-MBGNs) with either a positive, negative, or neutral charge by pre-osteoblasts and macrophages. These two cell types were selected since they i) orchestrate bone regeneration and ii) host persistent intracellular bacterial pathogens during bone infection.[23,24] Calcium was incorporated into the silica network in view of its well-known osteogenic capacity as well as its network-modifying capacity which facilitates the degradation of MBGNs.[25] Copper was introduced into the nanoparticles as a model antibacterial ion with broad-spectrum bactericidal efficacy.[26] Our group recently reported on the potent antibacterial properties of Cu-MBGNs (5 mol% of Cu) against Methicillin-resistant Staphylococcus aureus (MRSA).[27] In the current study, we investigated the release kinetics of these bioinorganic ions in more detail as a function of pH. Our quantitative and qualitative data showed that Cu-doped MBGNs were efficiently internalized and co-localized with lysosomes, irrespective of nanoparticle surface charge or cell type. We further confirmed that the Cu-MBGNs formed a protein corona, which determined nanoparticle-cell interactions rather than the properties of bare protein-free nanoparticles. In addition, the accelerated release of Si^{4+}, Ca^{2+}, and Cu^{2+} ions from nanoparticles under acidic conditions might be attributed to the pH-responsive behavior of these nanocarriers, which is beneficial for applications in bone infection or bone cancer characterized by tissue acidification. Finally, the ability of these nanocarriers to deliver their therapeutic cargos (including copper ions) to different cell types confirms their potential as intracellular delivery nanocarriers for application in bone substitutes.

Materials and Methods

Materials

All chemicals used for Cu-doped MBGNs synthesis were purchased from Sigma-Aldrich. Alpha minimum essential medium (α-MEM), RPMI 1640 cell culture medium, fetal bovine serum (FBS), penicillin/streptomycin, and trypsin/EDTA were purchased from Gibco (ThermoFisher Scientific, Waltham, MA, USA). Fluorescein isothiocyanate isomer I (FITC), Cell Counting Kit-8 (CCK-8), Trypan Blue, formalin, and Triton X-100 were purchased from Sigma-Aldrich (St. Louis, MO, USA). For confocal microscopy, µ-slide 8-well plates were acquired from Ibidi GmbH (Gräfelfing, Germany). Alexa Fluor 568 Phalloidin and 4′,6-diamidino-2-phenylindole (DAPI) were purchased from Sigma-Aldrich. LysoTracker® Red was provided by Invitrogen (ThermoFisher Scientific, Waltham, MA, USA). All chemicals and materials were used without any further purification.

Synthesis of Cu-Doped Mesoporous Bioactive Glass Nanoparticles

Cu-doped mesoporous bioactive glass (Cu-MBGNs) were synthesized via a microemulsion-assisted sol-gel method.[27] This entailed dissolving cetyltrimethylammonium bromide ($C_{19}H_{42}BrN$, CTAB, 0.56 g) in demineralized water (26 mL) under mild heating (50°C) to obtain a clear solution, and then adding ethyl acetate (8 mL) dropwise to start the formation of droplets. After 30 min, the pH was adjusted to 10–11 by adding ammonium hydroxide (25%) to the mixture. After 15 min, tetraethyl orthosilicate ($SiC_8H_{20}O_4$, TEOS, 3 mL), calcium nitrate tetrahydrate ($Ca\ (NO_3)_2.4H_2O$, 4.5 g), and copper (II) chloride dihydrate ($CuCl_2.\ 2H_2O$, 40 mg) were added sequentially to the mixture at intervals of 30 min. After 4h of mixing, the resulting blue precipitation was collected by centrifugation and washed with water and ethanol three times before the freeze-drying step. Afterward, the organic template and nitrates were removed by calcination of dry powders at 680°C for 6 h at a heating rate of 2°C/min.

Physicochemical Characterization of Cu-Doped Mesoporous Bioactive Glass Nanoparticles

The synthesized nanoparticles were subsequently characterized using various techniques. The morphology of nanoparticles was observed using a Field Emission Scanning Electron Microscope (FE-SEM; Sigma 300, Zeiss, Germany). The average size and size distribution of particles were determined by measuring the diameter of at least 100 particles using ImageJ software. The porous structure of nanoparticles was imaged using a Transmission Electron Microscope (TEM, JEOL JEM 1400, Japan). The hydrodynamic diameter of particles was determined using Dynamic Light Scattering (DLS, Malvern Zetasizer Nano-Z) for well-dispersed aqueous particle dispersions with three replications (n=3). The surface charge of synthesized nanoparticles dispersed in HEPES buffer (5 mM, pH=7.4) was measured using Laser Doppler Electrophoresis.

SEM equipped with an energy-dispersive X-ray detector (EDX) was utilized to analyze the elemental composition of nanoparticles. In addition, the chemical composition of nanoparticles was precisely determined using acid digestion and inductively coupled plasma-optical emission spectroscopy (ICP-OES, Perkin Elmer 8300 DV). For this measurement, Cu-MBGNs powder (100 mg) was mixed with anhydrous lithium metaborate ($BLiO_2$, 80% w/w) and lithium tetraborate ($Li_2B_4O_7$, 20% w/w) in a clean and dry platinum crucible. The crucible was then transferred to a furnace (XrFuse 2 Fusion machine) and fused at 1000°C for at least 30 min. The resulting mixture was subsequently dissolved in nitric acid (HNO_3, 2M) prior to ICP-OES analyses. Textural properties of nanoparticles were evaluated by nitrogen adsorption-desorption measurement using a high-performance micropore analyzer (Kubo X1000) in which synthesized Cu-MBGNs were degassed under vacuum for 4h, at 200°C prior to the analysis. The specific surface area (SSA_{BET}), pore size distribution, and pore volume were determined by means of the Brunauer-Emmett-Teller (BET) and the Barret-Joyner-Halenda (BJH) methods, respectively.

The molecular structure of the nanoparticles was assessed at room temperature by Fourier Transform Infrared Spectroscopy (FTIR, Spectrum One, Perkin Elmer) in the Attenuated Total Reflectance (ATR) mode (spectral range between 400–4000 cm^{-1}). Finally, to confirm the amorphous nature of the glass particles, an X-ray diffractometer (PW 1830, PANalytical X'Pert3 Powder) was conducted.

Preparation of Differently Charged Cu-Doped Mesoporous Bioactive Glass Nanoparticles

First, amine groups were conjugated to Cu-MBGNs using (3-aminopropyl) triethoxysilane (APTES). Cu-MBGNs were evenly dispersed in toluene (2 mg/mL) and then APTES (20% w/w) was added, and the reaction underwent reflux at 70 °C for 16 h. Next, the resulting product was collected and washed thoroughly with ethanol (96%, three times) and water (two times) to remove excess APTES. FTIR analysis and Laser Doppler Electrophoresis analyses were performed to confirm the amine functionalization process. In fact, the amine functionalization step was necessary not only to convert negatively charged Cu-MBGNs into positively charged nanoparticles but also to facilitate the following labeling step with FITC molecule through the formation of covalent and stable bonds, which could not be achieved through the physical adsorption of FITC to Cu-MBGNs. Moreover, this step allowed us to produce labeled negatively and neutrally charged Cu-MBGNs by optimizing the applied FITC content. Therefore, to prepare differently charged Cu-MBGNs, various ratios of FITC: Aminated Cu-MBGNs (1:5, 1:10, 1:20, 1:50, 1:100, and 1:200) were applied. This entailed adding a pre-determined amount of FITC to the well-dispersed amine-functionalized Cu-MBGNs (20 mg) in absolute ethanol and then, while avoiding light exposure, gently stirring the mixture for 12 h, while avoiding light exposure, to complete the reaction. Finally, labeled nanoparticles were washed three times with absolute ethanol by centrifugation for 30 min at 16,099 rcf and subsequently stored in absolute ethanol at room temperature (RT) until further usage. Among the aforementioned applied FITC: Aminated Cu-MBGNs ratios, 1:5, 1:20, and 1:100 resulted in negatively, neutrally, and positively charged nanoparticles.

Cell Culture Experiments

The murine pre-osteoblast cell line (MC3T3-E1) and RAW 264.7 macrophages were obtained from the American Type Culture Collection (ATCC) to culture them in α-MEM supplemented with 10% FBS and 1% penicillin/streptomycin (100

U/mL penicillin and 100 mg/mL streptomycin). The cells were then incubated in a humidified atmosphere at 37°C in 5% CO_2.

Cytotoxicity of Nanoparticles

To assess cell viability and evaluate the cytotoxicity of differently charged Cu-MBGNs, CCK-8 reagent was used. Cells were seeded in 48-well plates at a density of 1.7×10^4 cells/well and cultured in 300 µL of α-MEM growth medium at 37°C and 5% CO_2. After culturing for 24 h (MC3T3-E1) and 48 h (RAW 264.7), cells were washed with phosphate-buffered saline (PBS; pH 7.4) and exposed to 200 µL of growth medium containing different concentrations of nanoparticles (0, 25, 50, 75, 100, and 125 µg/mL) with various surface charges. After 24 h of exposure, cells were washed with PBS and 200 µL of growth medium containing CCK-8 reagent (10% v/v) was added to each well, followed by 4 h of incubation at 37°C. Afterward, the optical density (OD) value of the cells was measured at 450 nm using a SynergyTM HTX multi-mode microplate reader (BioTek Instruments Inc., Winooski, Vermont, USA). Relative cell viability is presented as the percentage of viable cells (n=3) normalized to the control (cells in basal medium without nanoparticles).

A higher concentration of Cu-MBGNs (>125 µg/mL) was not included in the cytotoxicity assessment, since due to the high solubility and/or reactivity of bioactive glasses, accumulation of ions in static cell culture conditions occurs which further increases the pH of the media and toxicity effect.[28,29] Moreover, introducing higher concentrations of nanoparticles was not necessary as the cellular uptake was not dose-dependent while adding higher concentrations of nanoparticles compromised the imaging quality.

Visualization of Cellular Uptake of Cu-Doped Mesoporous Bioactive Glass Nanoparticles

To visualize the cellular uptake of differently charged Cu-MBGNs, cells were seeded on Ibidi µ-slide 8-well plates at a density of 1.0×10^4 cells/well (MC3T3-E1) and 1.8×10^4 cells/well (RAW 264.7). Cells were cultured (up to a maximum of ~50% confluency to minimize the number of overlapping cells) for 24 h in 300 µL of growth medium at 37°C and 5% CO_2 to allow for cell adherence. After washing with PBS, cells were exposed to 200 µL growth medium containing 25 µg/mL of differently charged Cu-MBGNs. After 24 h, cells were washed with PBS and fixed with 3.7% formalin for 15 min at room temperature (RT). Samples were subjected to established immunofluorescence staining procedures. Briefly, cells were permeabilized using incubation with 0.1% Triton X-100 for 10 min at RT and treated with Alexa Fluor 568 Phalloidin (1:400) for 20 min at room temperature to achieve cytoskeletal F-actin staining. Cells were counterstained using 4′,6-diamidino-2-phenylindole (DAPI, 1:70). The internalization of nanoparticles was visualized using a confocal laser scanning microscope (CLSM, Leica TCS SP8 SMD, Germany). Alexa Fluor 568 and DAPI were excited at 578 nm (detection: 580–620 nm) and 405 nm (detection: 420–460 nm), respectively.

To investigate the potential co-localization of the Cu-MBGNs with cellular lysosomes, cells were stained with LysoTracker® after exposure to 25 µg/mL of nanoparticles. In brief, cells were washed with PBS 24 h after exposure to Cu-MBGNs and incubated with 50 nM LysoTracker® Red in RPMI 1640 medium without phenol red for 2 h. Confocal laser scanning microscopy was used to capture images, with nanoparticles and LysoTracker deep red excited at 488 nm (detection: 500–540 nm) and 633 nm (detection: 660–700 nm), respectively. Fiji was used for the reconstruction of images.

Internalization Efficiency of Cu-Doped Mesoporous Bioactive Glass Nanoparticles

In addition to validating the internalization of Cu-MBGNs microscopically, their uptake efficiency in MC3T3-E1 and RAW 264.7 cell types was determined. Cells were seeded in 48-well plates at a density of 1.7×10^4 cells/well and cultured in 300 µL of growth medium at 37°C and 5% CO_2. Cells were allowed to attach and form a confluent monolayer followed by washing with PBS and exposure to 200 µL growth medium containing 25 and 50 µg/mL of three differently charged Cu-MBGNs. After 4 h and 24 h of particle exposure, 25 µL of Trypan Blue solution was added to each well containing cells to quench non-internalized and membrane-bound nanoparticles.[30] Subsequently, fluorescent intensity

(FI) was measured at an excitation and emission wavelength of 485 nm and 528 nm, respectively. The percentage of internalized nanoparticles was calculated using the following formula:

$$\%\ \text{Internalized nanoparticles} = \frac{[\mathrm{FI}_{\text{experimental sample}}]}{[\mathrm{FI}_{\text{control}}]} \times 100\%$$

In this formula, FI experimental sample refers to the fluorescence intensity of a well containing cells exposed to nanoparticles and Trypan Blue, while FI control refers to the fluorescence intensity of a well without cells containing corresponding concentrations of nanoparticles in the growth medium. The results were presented as mean ± SD from triplicate wells (n=3). In addition, a standard curve of fluorescent intensity (FI) against nanoparticle concentration was plotted to confirm their linear relationship (Figure S1). A serial dilution of nanoparticles was prepared in concentrations of 0, 3.12, 6.25, 12.5, 25, 50, and 100 µg/mL in supplemented growth medium. After 24 h of incubation at 37°C, FI of the samples was measured at an excitation and emission wavelength of 485 nm and 528 nm, respectively.

Protein Corona Formation

To assess the formation of a protein corona on the surface of the nanoparticle, three types of differently charged Cu-MBGNs (50 µg/mL) were incubated in α-MEM containing 10% FBS. First, a stock dispersion of nanoparticles in demineralized water was prepared (5 mg/mL). Then, 200 µL of the premade stock was added to α-MEM containing 10% FBS to reach a final concentration of 500 µg/mL (n=3). After 4 h and 24 h of incubation at 37°C under gentle shaking, protein-nanoparticle complexes were collected by centrifugation (16,099 rcf) and washed three times with demineralized water to remove unbound and/or loosely bound proteins. The surface charge of three sets of nanoparticles dispersed in HEPES buffer (5 mM, pH=7.4) was measured using a Zetasizer apparatus. Nanoparticle surface charge was also measured after incubation in demineralized water for 4 h and 24 h to compare the effect of proteins present in culture media on nanoparticle surface properties.

In vitro Ionic Release Measurements

The time-dependent dissolution behavior of amine-functionalized Cu-MBGNs was studied in two different media, ie, PBS (pH 7.4) and artificial lysosomal fluid (ALF, pH 4.5). The chemical composition of ALF is presented in Table S1.[31] Briefly, 20 mg of nanoparticles (n=3) were immersed in 20 mL of PBS or ALF solution followed by incubation at 37°C under horizontal shaking at 120 rpm for up to 10 days. At each predetermined time point (1, 3, 5, 24, 48, 120, 168, and 240 h), samples were centrifuged for 20 min at 16,099 rcf and the supernatant was collected, and the media was refreshed. The collected aliquots were then diluted using nitric acid solutions (2%) and analyzed by inductively coupled plasma-mass spectrometry (ICP-MS) to determine the ionic concentration of Si, Ca, and Cu ions in the supernatant. Values obtained from negative control samples (ie, PBS and ALF without nanoparticles) were subtracted from all experimental sample values.

Detection of Intracellular Si, Ca, and Cu Ion Concentrations

To assess the capacity of Cu-MBGNs to deliver therapeutic ions intracellularly, MC3T3-E1 and RAW 264.7 cells were seeded in a 6 well-plate at a density of 15×10^4 and 20×10^4, respectively. After 24 h, cells were exposed to 50 µg/mL of amine-functionalized Cu-MBGNs (n=3). After another 24 h, the cells were washed with PBS to remove extracellular nanoparticles and media. To measure intracellular ion concentrations, the cells were detached and subjected to centrifugation (350 rcf, 5 min). Subsequently, cells were incubated in nitric acid (65%) for 3 h at 150°C and subsequently cooled down to room temperature. The resulting samples were then diluted with demineralized water (to reach 2% nitric acid in the final sample) to measure Si, Ca, and Cu ion concentrations using ICP-MS analysis. The same experimental work was performed for both cell types without treatment with Cu-MBGNs.

Statistical Analysis

Data are presented as the mean ± standard deviation (SD) for the indicated number of independent experiments. Statistical analysis of data was performed with a one-way analysis of variance (ANOVA) followed by a Tukey-HSD post hoc test for multiple comparisons (IBM SPSS Statistics for Windows, Version 25.0). P-values lower than 0.05 were considered statistically significant.

Results and Discussion

First, monodispersed Cu-doped MBGNs (Cu-MBGNs) were synthesized through a microemulsion-assisted sol-gel technique, as previously reported.[27] The uniform spherical morphology and radial porosity of synthesized nanoparticles were confirmed using SEM and TEM, respectively (Figure 1A and B). The obtained nanoparticles had an average size of 103 ± 10 nm (dry state, Figure 1C) and a hydrodynamic size of 165 ± 5 nm (Table 1). The synthesized nanoparticles had a negative surface charge of −19.4 ± 0.8 mV. EDX analysis confirmed the presence of Si, Ca, and Cu (Figure S1), while ICP-OES analysis revealed that the Cu-MBGNs were composed of 86.4 mol% of SiO_2, 9.5 mol% of CaO, and 4.1 mol% of CuO (Table 1). This elemental composition was optimized in a previous study conducted by our group, which confirmed the potent antibacterial efficacy of nanoparticles with similar composition against MRSA bacteria involved in severe bone infection.[27] The mesoporous structure of synthesized Cu-MBGNs was studied in more detail using nitrogen adsorption analysis. Figure 1D shows nitrogen adsorption-desorption isotherms of nanoparticles, indicating a type IV isotherm which is typical for mesoporous materials. The nanoparticles showed a narrow pore size distribution centered around 3.1 nm (as shown in the insert in Figure 1D) and a large specific surface area of about 253 m^2/g (Table 1), which may enable them to carry large loads of therapeutic ions/drugs. We further analyzed the molecular structure of Cu-MBGNs using FTIR analysis, which revealed Si–O–Si bending and symmetric stretching vibrations characteristic for silicate glasses ~450 and ~800 cm^{-1}, respectively (Figure 1E). The corresponding XRD pattern presented in Figure 1F confirms the amorphous structure of the synthesized nanoparticles since only one broad band located at $2\theta=23^\circ$ was observed which is attributed to silicate-based glasses.[6,32]

The surface charge of nanocarriers is one of the most influential factors affecting their interaction with cells, and subsequently, their therapeutic efficacy. The generally accepted theory regarding the favorable internalization of positively charged nanoparticles seems overly simplistic, as negatively charged particles have also been reported to efficiently cross the cell membrane.[8,11,33] Therefore, three groups of nanoparticles with either a positive, neutral or negative surface charge

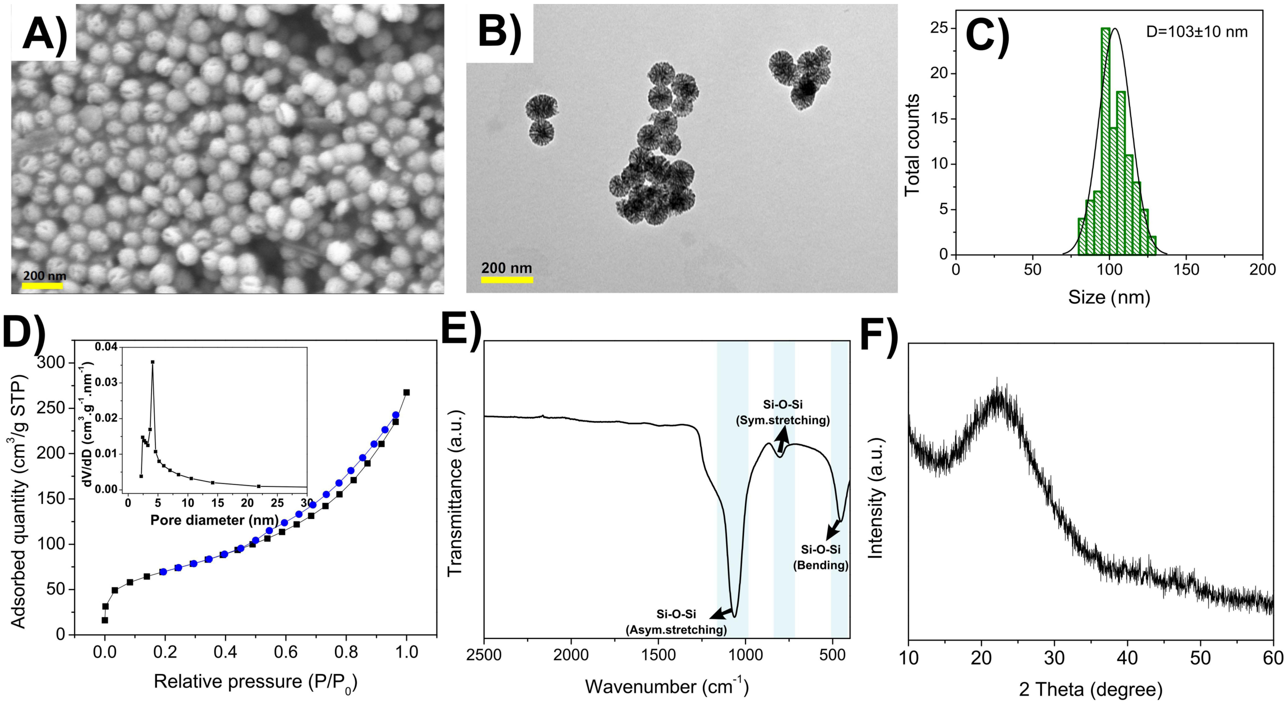

Figure 1 Synthesis and characterization of Cu-MBGNs. (**A**) SEM and (**B**) TEM of Cu-MBGNs. (**C**) Size distribution of Cu-MBGNs obtained from SEM pictures. (**D**) Nitrogen adsorption-desorption isotherms and pore size distribution (insert) of Cu-MBGNs. (**E**) FTIR spectra and (**F**) XRD patterns of synthesized nanoparticles.

Table 1 Chemical Compositions, Textural and Surface Properties of Synthesized Cu-MBGNs. SSA Refers to the Specific Surface Area of the Nanoparticles

Chemical Composition (mol%)	Zeta Potential (mV)	DLS Size (nm)	SSA (m^2/g)	Pore Volume (cm^3/g)	Pore Size (nm)
86.4 SiO_2-9.5 CaO- 4.1 CuO	−19.4 ± 0.8	165 ± 5	253	0.41	3.11

were prepared to study the exact effect of surface charge on the internalization ability of Cu-MBGNs. First, a post-synthesis procedure was performed by conjugation of APTES (Scheme 1) to the obtained Cu-MBGNs, which resulted in amine-functionalized nanoparticles and shifted their surface charge from −19.4 ± 0.8 mV to +22.5 ± 0.6 mV. A new peak in the FTIR spectrum located at ~1640 cm^{-1} appeared (Figure 2B), corresponding to the bending vibration of the N-H bond, indicating successful conjugation of amine groups to the nanoparticles.[34] In the next step, different ratios of FITC: Aminated Cu-MBGNs (w/w) were applied to prepare differently charged nanoparticles that were fluorescently labeled to monitor cellular uptake. As shown in Figure 2C, the reaction between the isothiocyanate group present in FITC and amine groups present in amine-functionalized Cu-MBGNs can alter the surface charge of nanoparticles depending on the applied amount of FITC. Therefore, positively charged Cu-MBGNs were obtained by applying a FITC: Aminated Cu-MBGN ratio of 1:100, as this ratio preserves the initial surface charge of amine-functionalized nanoparticles. However, 1:5 and 1:50 ratios resulted in negatively (– 17.8 ± 0.9) and almost neutrally charged (+ 4.4 ± 0.4) Cu-MBGNs (Table 2).

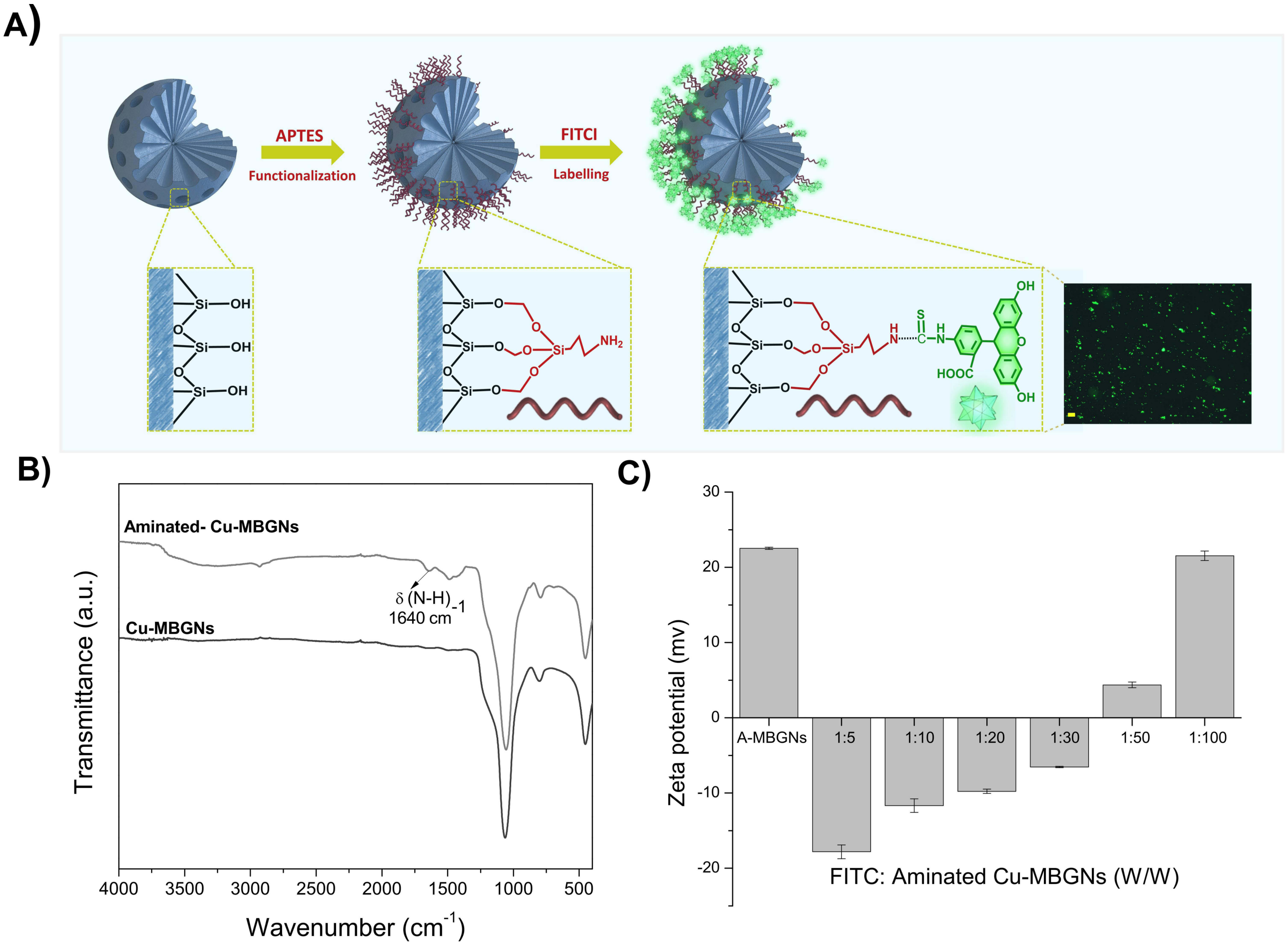

Figure 2 (**A**) Schematic illustration indicating preparation of differently charged Cu-MBGNs through surface modification with APTES and labeling with FITC. (**B**) FTIR spectra of Cu-MBGNs before and after amine modification. (**C**) Variation of the surface charge of aminated Cu-MBGNs depending on the applied FITC: aminated Cu-MBGNs ratio. The scale bar in panel A represents 20 μm.

Table 2 Surface Charge of Three Groups of Cu-MBGNs

Groups	FITC: Aminated Cu-MBGNs (w/w)	Surface Charge (mV)
Negatively charged Cu-MBGNs	1:5	−17.8 ± 0.9
Neutrally charged Cu-MBGNs	1:50	+ 4.4 ± 0.4
Positively charged Cu-MBGNs	1:100	+ 22.5 ± 0.6

The interaction of synthesized Cu-MBGNs with MC3T3-E1 pre-osteoblasts and RAW 264.7 macrophages was first investigated by assessing the cytotoxicity of the particles for both cell types. Cells were exposed to differently charged Cu-MBGNs at low concentrations, ranging from 0 to 125 µg/mL for 24 h without a prior preconditioning step of nanoparticles, whereafter their cell viability was measured using the CCK-8 assay. Figure 3A and B show that the nanoparticles were not toxic ($P > 0.05$) for both cell types at all tested nanoparticle concentrations.

To efficiently deliver their therapeutic cargo, intracellular nanocarriers should be readily internalized. Therefore, confocal microscopy was performed to visualize the cellular uptake of Cu-MBGNs by Both MC3T3-E1 and RAW 264.7 which were exposed to differently charged Cu-MBGNs for 24 h. As shown in Figure 3C, all nanoparticles were detected intracellularly in close proximity to the cell nucleus for both cell types. The green-labeled nanoparticles were mainly observed inside the cells and not bound to the cell membrane, as confirmed by the z-stacks represented in the supporting information (Supplementary Videos 1, 2, 3, 4, 5 and 6).

We further attempted to quantitatively compare the internalization efficacy of three sets of Cu-MBGNs in order to elucidate if the surface charge of the pristine nanocarriers determines cellular uptake. This was accomplished by measuring the fluorescence intensity of cells (MC3T3-E1 and RAW 264.7) exposed to the differently charged nanoparticles at concentrations of 25 and 50 µg/mL after 4 h and 24 h. The linear relationship between fluorescence intensity and the concentration of Cu-MBGNs was confirmed by obtaining a standard curve for all three sets of nanoparticles (Figure S2). Trypan blue was used to ensure that only internalized nanoparticles were quantified due to its known FITC-quenching effect since trypan blue cannot pass the intact membrane of viable cells, thereby quenching extracellular fluorescence only.[30,35] Both RAW 264.7 and MC3T3-E1 internalized ~30% of the Cu-MBGNs nanoparticles irrespective of the incubation time, nanoparticle concentration, and surface charge (Figure 3D and E). Phagocytosis could be considered as the uptake pathway of Cu-MBGNs into

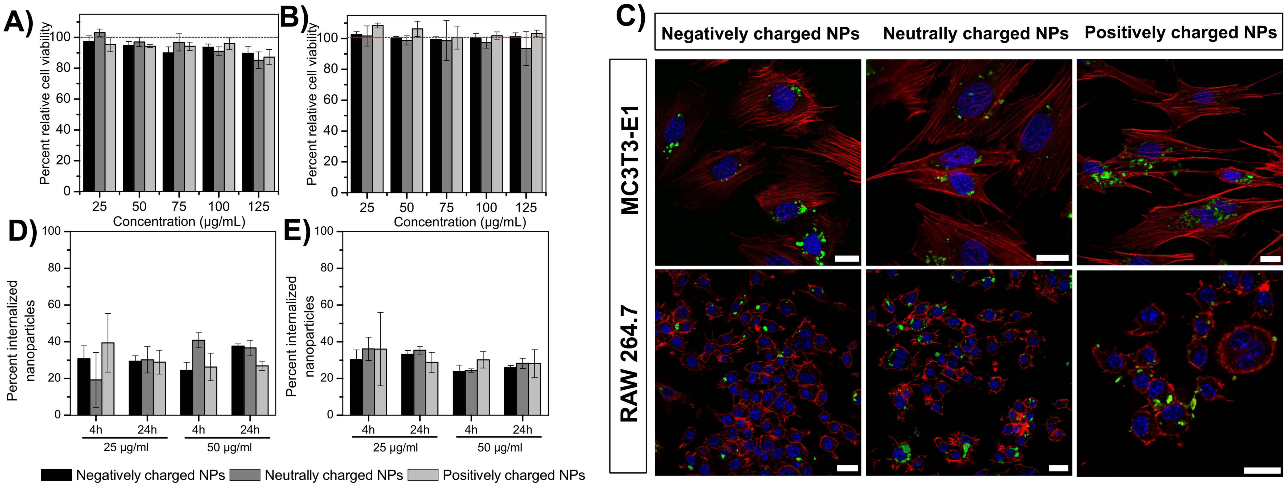

Figure 3 Interaction between differently charged Cu-MBGNs with MC3T3-E1 and RAW 264.7 cells. Cytocompatibility of differently charged Cu-MBGN to (**A**) MC3T3-E1 and (**B**) RAW 264.7 cells as a function of nanoparticle concentration. Dashed red lines in panel A and B indicate the control group (cells without particles). (**C**) Intracellular uptake of differently charged Cu-MBGNs by MC3T3-E1 and RAW 264.7 cells. Cu-MBGNs were labeled using FITC (green), while actin filaments of the cytoskeleton and nuclei were stained with rhodamine-phalloidin (red) and DAPI (blue), respectively. Intracellular uptake efficiency of differently charged Cu-MBGNs by (**D**) MC3T3-E1 and (**E**) RAW 264.7 cells. Scale bars represent 10 µm.

macrophages, as this pathway is generally involved in the internalization of large particles (>500 nm). The presence of Cu-MBGN clusters inside the RAW cells and in culture media suggests the probability of Cu-MBGN aggregations, which was confirmed by DLS data presenting a "secondary size" for the particles in cell culture media.[21] Interestingly, MC3T3-E1 cells, not specialized in phagocytosis, were also capable of internalizing Cu-MBGNs in all three sets of nanoparticles to a similar extent as RAW 264.7 cells, which are considered professional phagocytes. This similarity in internalization of Cu-MBGNs strongly implies that the cellular uptake of nanoparticles is a complex interplay of multiple factors that cannot be predicted by individual characteristics such as nanoparticle charge.[36] The involvement of ATP-dependent endocytosis has been already reported for MBGNs with comparable surface properties with our synthesized nanoparticles. Among the tested pathways, micropinocytosis was found to be the major pathway for MBGN internalization by non-phagocytic cells.[8]

The effect of protein adsorption on particle surface charge was studied in order to explain why nanoparticle surface charge apparently did not affect the cellular uptake of nanoparticles. Proteins are abundantly present in physiological fluids such as blood, interstitial fluid, and the cytoplasm, resulting in rapid protein adsorption onto the surface of nanoparticles. This alters their physicochemical properties, including size, zeta potential, and aggregation state.[37] Therefore, three different groups of Cu-MBGNs were dispersed in either culture medium supplemented with FBS or in demineralized water for both 4 h and 24 h. As shown in Figure 4, the surface zeta potential for each group of nanoparticles was initially distinct (ranging from −17.8 ± 0.9 mV to 22.5 ± 0.6 mV) but shifted to a negative zeta potential for all groups irrespective of their initial surface charge after 4 h of immersion in media containing serum proteins (FBS).

These data clearly confirm the formation of a negatively charged protein corona surrounding the Cu-MBGNs within 4 h of incubation, the charge of which did not change at a longer exposure time of 24 h (Figure S3). However, the surface charge of nanoparticles dispersed in demineralized water remained intact after 4 h and 24 h of incubation (Figure S4). Physicochemical characteristics of nanoparticles such as hydrophobicity and initial surface charge influence the protein corona formation.[38,39] The presence of more hydrophilic groups (hydroxyl and carboxyl) on negatively and neutrally charged Cu-MBGNs attenuated the protein adsorption compared to the positively charged particles. Besides hydrophobic interactions, proteins can undergo charge-driven binding to the nanoparticle interface. Since albumin, one of the most

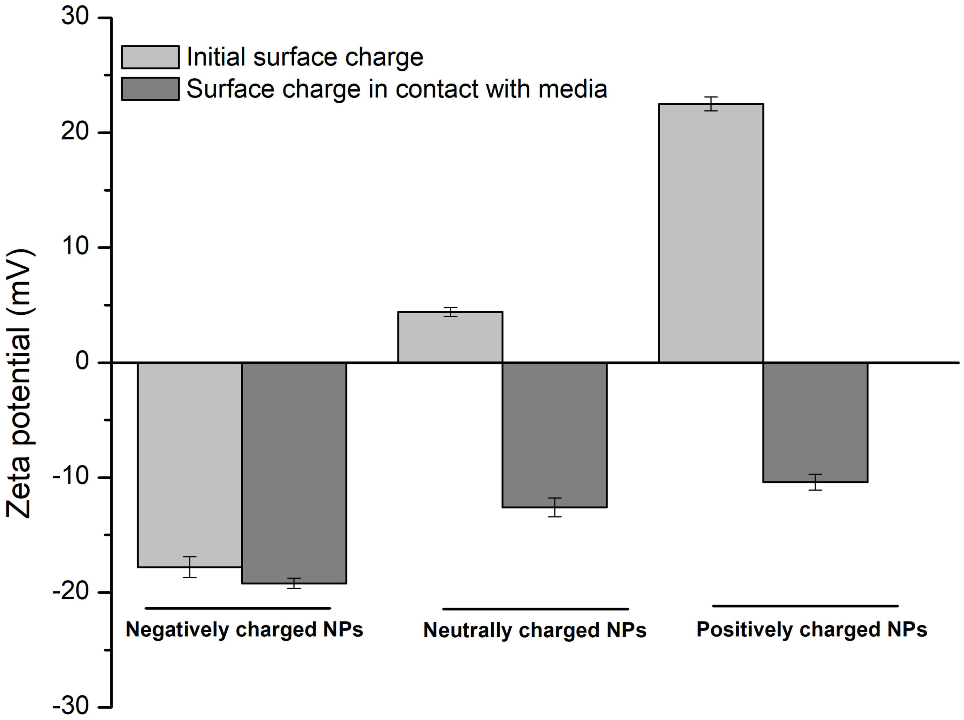

Figure 4 Zeta potential measurement of the nanoparticles after 4 h of incubation in media containing FBS.

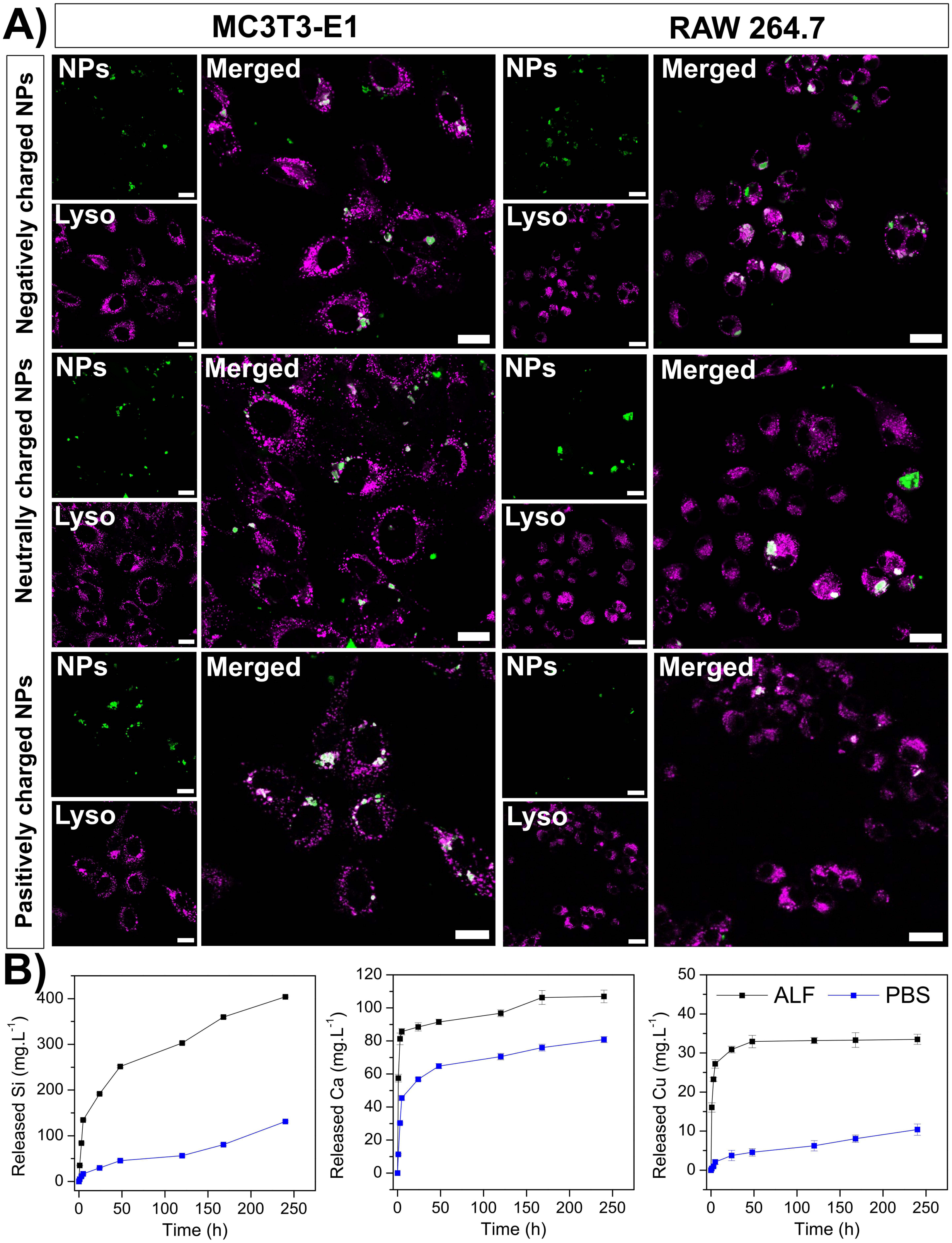

Figure 5 (**A**) Colocalization of Cu-MBGNs. MC3T3-E1 and RAW 264.7 cells were treated with differently charged Cu-MBGNs for 24 h and then stained with LysoTracker® Red. Scale bars represent 10 μm. (**B**) In vitro ion release profiles of Cu-MBGNs in PBS and ALF for up to 10 days.

abundant proteins in blood plasma and FBS, has a slightly negative net charge (isoelectric point= 4.7), adsorption to positively charged Cu-MBGNs is likely to occur to a greater extent.[39] Collectively, our results confirm that the surface charge of the nanoparticles is dynamic and depends on the composition of biological media. Therefore, the charge of the protein coating/corona, rather than the native particle surface charge, does eventually determine the interaction between nanoparticles and cells. This finding should be considered in future studies on the cellular uptake of MBGN-based nanocarriers.

The suitability of nanocarriers is not only determined by their internalization ability, but also by their ability to release their therapeutic cargo intracellularly. Therefore, we further investigated the intracellular fate of internalized nanoparticles affecting the efficacy of intracellular cargo release. Since nanocarriers are often localized in acidic vehicles such as endosomes and/or lysosomes,[40] MC3T3-E1 and RAW 264.7 were exposed to Cu-MBGNs with different surface charges and subsequently stained by LysoTracker® Red as organelle-specific fluorescent marker. Merged live-cell images revealed that internalized Cu-MBGNs mostly colocalized with lysosomes after 24 h of incubation (as shown in Figure 5A). Our data are in line with several studies by other groups reporting the localization of silica nanoparticles in lysosomes without any signs of endosomal escape from this location.[41–43]

By confirming the trafficking of the nanoparticles from the extracellular environment (pH 7.4) into late endosomes/lysosomes (pH 4.5), we confirmed that nanoparticles will be in contact with compartmentalized environments of reduced pH. Therefore, we investigated their ability as intracellular carriers for the delivery of therapeutic ions like Cu^{2+} and Ca^{2+} to stimulate osteogenesis or combat intracellular bacteria. Using ICP-MS analysis, the release behavior of aminated Cu-MBGNs was studied in artificial lysosomal fluid (ALP, pH=4.5) and PBS (pH=7.4) for 10 days. As shown in Figure 5B, at both pH values, the first stage of silica dissolution, corresponding to disruption of the outer layer of the silica network, resulted in an initial fast release that was then followed by a more gradual release up to 10 days. In contrast, a fast release of Ca^{2+} and Cu^{2+} ions within the first day at both pH values was observed. This fast release rate could be attributed to the relatively rapid diffusion of these ions from the outer part of the nanoparticles, as well as to the small dimensions of these ions (~0.1–0.2 nm) as compared to the pore size of nanoparticles (~ 3nm).[32] The release data confirmed the ability of MBGNs to deliver their cargos to the extracellular and lysosomal environment. The higher released content of Si^{4+}, Ca^{2+}, and Cu^{2+} in ALF compared to SBF could be related to various factors, such as the difference in the chemical composition of both buffers and/or the low pH of ALF due to the presence of a high concentration of protons accelerating the ion exchange with bioactive glass.[44,45]

The ability of Cu-MBGNs to deliver therapeutic ions intracellularly was further assessed as Si^{4+}, Ca^{2+}, and Cu^{2+} ions strongly affect osteogenesis, angiogenesis, and inhibition of bacterial activity. MC3T3-E1 and RAW 264.7 were treated with aminated Cu-MBGNs (50 µg/mL) for 24 h and the intracellular level of different ions was quantified by ICP-MS. The presence of all ions (including Cu^{2+}) was detected inside the cells (see Table 3). These data suggest that Cu-MBGNs can be used to efficiently deliver Cu^{2+} inside cells. This paves the way for future in vitro and in vivo studies evaluating the capacity of these nanocarriers to efficiently kill intracellular bacteria and combat severe bone infections. In addition, the authors suggest that further studies on the fundamental internalization pathways of Cu-MBGNs are required to elaborate on the observed similarity in the internalization efficacy of Cu-MBGNs by macrophages and preosteoclasts.

Table 3 Intracellular Level of Different Ions in Treated and Non-Treated MC3T3-E1 and RAW 264.7

Cell Type	Si^{4+} (ppb)	Ca^{2+} (ppb)	Cu^{2+} (ppb)
MC3T3-E1-treated	38.4±8.3	20.2±4.3	2.3±0.4
MC3T3-E1-non-treated	0.24±0.05	<0.02	<0.001
RAW 264.7-treated	50.9±9.0	26.7±5.3	2.8±0.5
RAW 264.7- non-treated	0.08±0.01	<0.01	<0.002

Conclusion

In summary, this study demonstrated the internalization of Cu-doped mesoporous bioactive glass nanoparticles (Cu-MBGNs) by MC3T3-E1 and RAW 264.7 cells, regardless of the surface charge of nanoparticles. The observed similarity in uptake efficiency was attributed to the formation of a protein corona in protein-rich cell culture media, resulting in a negative charge for all Cu-MBGNs, irrespective of their original surface charge. These results emphasize the multi-faceted nature of the cellular uptake process, which cannot be predicted solely based on the initial nanocarrier surface properties. Furthermore, the ability of Cu-doped MBGNs to deliver their therapeutic cargo, i.e. copper ions, intracellularly underscores their potential as effective nanocarriers for combatting intracellular infections. Future preclinical studies should investigate the capacity of these nanoparticles to eradicate intracellular bacterial pathogens using physiologically relevant in vitro and in vivo models for intracellular infections.

Acknowledgments

The authors would like to thank Caroline Lievens and Yi Zuo for their support in ICP analysis and BET measurement.

Funding

This work was financially supported by the Radboud Institute for Molecular Life Science (RIMLS) of Radboudumc.

Disclosure

The authors report no conflicts of interest in this work.

References

1. Baeza A, Ruiz-Molina D, Vallet-Regí M. Recent advances in porous nanoparticles for drug delivery in antitumoral applications: inorganic nanoparticles and nanoscale metal-organic frameworks. *Expert Opin Drug Deliv*. 2017;14(6):783–796. doi:10.1080/17425247.2016.1229298
2. Farjadian F, Ghasemi S, Akbarian M, Hoseini-Ghahfarokhi M, Moghoofei M, Doroudian M. Physically stimulus-responsive nanoparticles for therapy and diagnosis. *Front Chem*. 2022;10. doi:10.3389/fchem.2022.952675
3. Chou LY, Ming K, Chan WC. Strategies for the intracellular delivery of nanoparticles. *Chem Soc Rev*. 2011;40(1):233–245. doi:10.1039/c0cs00003e
4. Bari A, Bloise N, Fiorilli S, et al. Copper-containing mesoporous bioactive glass nanoparticles as multifunctional agent for bone regeneration. *Acta Biomater*. 2017;55:493–504. doi:10.1016/j.actbio.2017.04.012
5. Zhang Y, Hu M, Zhang W, Zhang X. Construction of tellurium-doped mesoporous bioactive glass nanoparticles for bone cancer therapy by promoting ROS-mediated apoptosis and antibacterial activity. *J Colloid Interface Sci*. 2022;610:719–730. doi:10.1016/j.jcis.2021.11.122
6. Zheng K, Balasubramanian P, Paterson TE, et al. Ag modified mesoporous bioactive glass nanoparticles for enhanced antibacterial activity in 3D infected skin model. *Mater Sci Eng C*. 2019;103:109764. doi:10.1016/j.msec.2019.109764
7. Zheng K, Torre E, Bari A, et al. Antioxidant mesoporous Ce-doped bioactive glass nanoparticles with anti-inflammatory and pro-osteogenic activities. *Mater Today Bio*. 2020;5:100041. doi:10.1016/j.mtbio.2020.100041
8. Lee J-H, Mandakhbayar N, El-Fiqi A, Kim H-W. Intracellular co-delivery of Sr ion and phenamil drug through mesoporous bioglass nanocarriers synergizes BMP signaling and tissue mineralization. *Acta Biomater*. 2017;60:93–108. doi:10.1016/j.actbio.2017.07.021
9. Kurtuldu F, Mutlu N, Michálek M, et al. Cerium and gallium containing mesoporous bioactive glass nanoparticles for bone regeneration: bioactivity, biocompatibility and antibacterial activity. *Mater Sci Eng C*. 2021;124:112050. doi:10.1016/j.msec.2021.112050
10. El-Fiqi A, Kim T-H, Kim M, et al. Capacity of mesoporous bioactive glass nanoparticles to deliver therapeutic molecules. *Nanoscale*. 2012;4(23):7475–7488. doi:10.1039/C2NR31775C
11. Sui B, Liu X, Sun J. Dual-functional dendritic mesoporous bioactive glass nanospheres for calcium influx-mediated specific tumor suppression and controlled drug delivery in vivo. *ACS Appl Mater Interfaces*. 2018;10(28):23548–23559. doi:10.1021/acsami.8b05616
12. Wu C, Fan W, Chang J. Functional mesoporous bioactive glass nanospheres: synthesis, high loading efficiency, controllable delivery of doxorubicin and inhibitory effect on bone cancer cells. *J Mater Chem B*. 2013;1(21):2710–2718. doi:10.1039/C3TB20275E
13. Wang X, Zhang Y, Lin C, Zhong W. Sol-gel derived terbium-containing mesoporous bioactive glasses nanospheres: in vitro hydroxyapatite formation and drug delivery. *Colloids Surf B*. 2017;160:406–415. doi:10.1016/j.colsurfb.2017.09.051
14. Gao Y, Chen Y, Cao Y, Mo A, Peng Q. Potentials of nanotechnology in treatment of methicillin-resistant Staphylococcus aureus. *Eur J Med Chem*. 2021;213:113056. doi:10.1016/j.ejmech.2020.113056
15. Gimza BD, Cassat JE. Mechanisms of antibiotic failure during Staphylococcus aureus osteomyelitis. *Front Immunol*. 2021;12. doi:10.3389/fimmu.2021.638085
16. Donahue ND, Acar H, Wilhelm S. Concepts of nanoparticle cellular uptake, intracellular trafficking, and kinetics in nanomedicine. *Adv Drug Deliv Rev*. 2019;143:68–96. doi:10.1016/j.addr.2019.04.008
17. Farjadian F, Roointan A, Mohammadi-Samani S, Hosseini M. Mesoporous silica nanoparticles: synthesis, pharmaceutical applications, biodistribution, and biosafety assessment. *J Chem Eng*. 2019;359:684–705.
18. Foroozandeh P, Aziz AA. Insight into cellular uptake and intracellular trafficking of nanoparticles. *Nanoscale Res Lett*. 2018;13(1):339. doi:10.1186/s11671-018-2728-6

19. Lee JH, Kang MS, Mahapatra C, Kim HW. Effect of aminated mesoporous bioactive glass nanoparticles on the differentiation of dental pulp stem cells. *PLoS One*. 2016;11(3):e0150727. doi:10.1371/journal.pone.0150727
20. Graf C, Gao Q, Schütz I, et al. Surface functionalization of silica nanoparticles supports colloidal stability in physiological media and facilitates internalization in cells. *Langmuir*. 2012;28(20):7598–7613. doi:10.1021/la204913t
21. Saikia J, Yazdimamaghani M, Hadipour Moghaddam SP, Ghandehari H. Differential protein adsorption and cellular uptake of silica nanoparticles based on size and porosity. *ACS Appl Mater Interfaces*. 2016;8(50):34820–34832. doi:10.1021/acsami.6b09950
22. Chen Y-P, Chen H-A, Hung Y, Chien F-C, Chen P, Mou C-Y. Surface charge effect in intracellular localization of mesoporous silica nanoparticles as probed by fluorescent ratiometric pH imaging. *RSC Adv*. 2012;2(3):968–973. doi:10.1039/C1RA00586C
23. Yahara Y, Ma X, Gracia L, Alman BA. Monocyte/macrophage lineage cells from fetal erythromyeloid progenitors orchestrate bone remodeling and repair. *Front Cell Dev Biol*. 2021;9. doi:10.3389/fcell.2021.622035
24. Kamaruzzaman NF, Kendall S, Good L. Targeting the hard to reach: challenges and novel strategies in the treatment of intracellular bacterial infections. *Br J Pharmacol*. 2017;174(14):2225–2236. doi:10.1111/bph.13664
25. Greasley SL, Page SJ, Sirovica S, et al. Controlling particle size in the Stöber process and incorporation of calcium. *J Colloid Interface Sci*. 2016;469:213–223. doi:10.1016/j.jcis.2016.01.065
26. Wang P, Yuan Y, Xu K, et al. Biological applications of copper-containing materials. *Bioact Mater*. 2021;6(4):916–927. doi:10.1016/j.bioactmat.2020.09.017
27. Hosseini M, Hassani Besheli N, Deng D, et al. Facile post modification synthesis of copper-doped mesoporous bioactive glass with high antibacterial performance to fight bone infection. *Biomater Adv*. 2023;144:213198. doi:10.1016/j.bioadv.2022.213198
28. Ciraldo FE, Boccardi E, Melli V, Westhauser F, Boccaccini AR. Tackling bioactive glass excessive in vitro bioreactivity: preconditioning approaches for cell culture tests. *Acta Biomater*. 2018;75:3–10. doi:10.1016/j.actbio.2018.05.019
29. Hohenbild F, Arango-Ospina M, Moghaddam A, Boccaccini AR, Westhauser F. Preconditioning of bioactive glasses before introduction to static cell culture: what is really necessary? *Methods Protoc*. 2020;3:2. doi:10.3390/mps3020038
30. Shilova ON, Shilov ES, Deyev SM. The effect of trypan blue treatment on autofluorescence of fixed cells. *Cytometry A*. 2017;91(9):917–925. doi:10.1002/cyto.a.23199
31. Naruphontjirakul P, Porter AE, Jones JR. In vitro osteogenesis by intracellular uptake of strontium containing bioactive glass nanoparticles. *Acta Biomater*. 2018;66:67–80. doi:10.1016/j.actbio.2017.11.008
32. Zheng K, Kang J, Rutkowski B, et al. Toward highly dispersed mesoporous bioactive glass nanoparticles with high cu concentration using Cu/ascorbic acid complex as precursor. *Front Chem*. 2019;7. doi:10.3389/fchem.2019.00497
33. Slowing II, Trewyn BG, Lin VSY. Mesoporous silica nanoparticles for intracellular delivery of membrane-impermeable proteins. *J Am Chem Soc*. 2007;129(28):8845–8849. doi:10.1021/ja0719780
34. Daryasari MP, Akhgar MR, Mamashli F, Bigdeli B, Khoobi M. Chitosan-folate coated mesoporous silica nanoparticles as a smart and pH-sensitive system for curcumin delivery. *RSC Adv*. 2016;6(107):105578–105588. doi:10.1039/C6RA23182A
35. Karpowicz RJ Jr, Haney CM, Mihaila TS, Sandler RM, Petersson EJ, Lee VM. Selective imaging of internalized proteopathic α-synuclein seeds in primary neurons reveals mechanistic insight into transmission of synucleinopathies. *J Biol Chem*. 2017;292(32):13482–13497. doi:10.1074/jbc.M117.780296
36. Ritz S, Schöttler S, Kotman N, et al. Protein corona of nanoparticles: distinct proteins regulate the cellular uptake. *Biomacromolecules*. 2015;16(4):1311–1321. doi:10.1021/acs.biomac.5b00108
37. Aggarwal P, Hall JB, McLeland CB, Dobrovolskaia MA, McNeil SE. Nanoparticle interaction with plasma proteins as it relates to particle biodistribution, biocompatibility and therapeutic efficacy. *Adv Drug Deliv Rev*. 2009;61(6):428–437. doi:10.1016/j.addr.2009.03.009
38. Yu Q, Zhao L, Guo C, Yan B, Su G. Regulating protein corona formation and dynamic protein exchange by controlling nanoparticle hydrophobicity. *Front Bioeng Biotechnol*. 2020;8. doi:10.3389/fbioe.2020.00210
39. Pustulka SM, Ling K, Pish SL, Champion JA. Protein nanoparticle charge and hydrophobicity govern protein corona and macrophage uptake. *ACS Appl Mater Interfaces*. 2020;12(43):48284–48295. doi:10.1021/acsami.0c12341
40. Xie S, Tao Y, Pan Y, et al. Biodegradable nanoparticles for intracellular delivery of antimicrobial agents. *J Control Release*. 2014;187:101–117. doi:10.1016/j.jconrel.2014.05.034
41. Sun J, Liu Y, Ge M, et al. A distinct endocytic mechanism of functionalized-silica nanoparticles in breast cancer stem cells. *Sci Rep*. 2017;7(1):16236. doi:10.1038/s41598-017-16591-z
42. Wu C, Wu Y, Jin Y, et al. Endosomal/lysosomal location of organically modified silica nanoparticles following caveolae-mediated endocytosis. *RSC Adv*. 2019;9(24):13855–13862. doi:10.1039/C9RA00404A
43. Shapero K, Fenaroli F, Lynch I, Cottell DC, Salvati A, Dawson KA. Time and space resolved uptake study of silica nanoparticles by human cells. *Mol Biosyst*. 2011;7(2):371–378. doi:10.1039/C0MB00109K
44. Bingel L, Gróh D, Karpukhina N, Brauer DS. Influence of dissolution medium pH on ion release and apatite formation of Bioglass® 45S5. *Mater Lett*. 2015;143:279–282. doi:10.1016/j.matlet.2014.12.124
45. Nommeots-Nomm A, Hupa L, Rohanová D, Brauer DS. A review of acellular immersion tests on bioactive glasses—influence of medium on ion release and apatite formation. *Int J Appl Glass Sci*. 2020;11(3):537–551. doi:10.1111/ijag.15006